

Shedding Light on Solid Sorbents: Evaluation of Supported Potassium Carbonate Particle Size and Its Effect on CO₂ Capture from Air

Nazila Masoud,* Victorien Clement, Tomas van Haasterecht, Marlene Führer, Jan P. Hofmann, and Johannes Hendrik Bitter*



Cite This: *Ind. Eng. Chem. Res.* 2022, 61, 14211–14221



Read Online

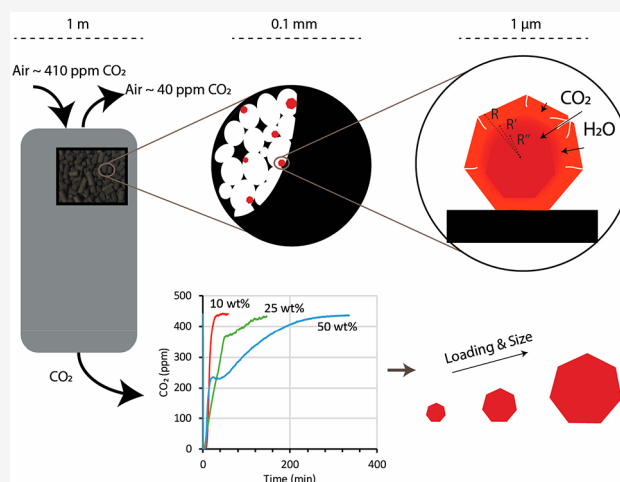
ACCESS |

Metrics & More

Article Recommendations

Supporting Information

ABSTRACT: Solid sorbents are essential for developing technologies that directly capture CO₂ from air. In solid sorbents, metal oxides and/or alkali metal carbonates such as potassium carbonate (K₂CO₃) are promising active components owing to their high thermal stability, low cost, and ability to chemisorb the CO₂ present at low concentrations in air. However, this chemisorption process is likely limited by internal diffusion of CO₂ into the bulk of K₂CO₃. Therefore, the size of the K₂CO₃ particles is expected to be an important factor in determining the kinetics of the sorption process during CO₂ capture. To date, the effects of particle size on supported K₂CO₃ sorbents are unknown mainly because particle sizes cannot be unambiguously determined. Here, we show that by using a series of techniques, the size of supported K₂CO₃ particles can be established. We prepared size-tuned carbon-supported K₂CO₃ particles by tuning the K₂CO₃ loading. We further used melting point depression of K₂CO₃ particles to collectively estimate the average K₂CO₃ particle sizes. Using these obtained average particle sizes, we show that the particle size critically affects the efficiency of the sorbent in CO₂ capture from air and directly affects the kinetics of CO₂ sorption as well as the energy input needed for the desorption step. By evaluating the mechanisms involved in the diffusion of CO₂ and H₂O into K₂CO₃ particles, we relate the microscopic characteristics of sorbents to their macroscopic performance, which is of interest for industrial-scale CO₂ capture from air.



1. INTRODUCTION

In heterogeneous catalysis, it is well-known that the size of the active component can affect a catalyst's performance via geometric and electronic effects.^{1,2} For instance, smaller supported metal nanoparticles have more low-coordinate corner and edge sites and fewer planar sites than larger particles. These two types of sites show different catalytic activities. For instance, corner and edge sites are the most active for CO oxidation by gold catalysts; thus, smaller particles are desired for this application.¹ Conversely planar sites are more active for propylene epoxidation by silver catalysts, so larger particles are desired.³ The reason for this difference is that the low-coordinate sites have more dangling bonds than planar sites and therefore exhibit different reactivity. Moreover, below 2 nm, the band structure of the particle changes to a more discrete orbital structure that alters the electronic properties and thus the reactivity of the particles. Though the effect of particle size on catalysts has been well studied, little is known about the particle size effect on the performance of a similar category of materials, namely, solid

sorbents, in which a solute reacts with the sorbent's active component that is dispersed over a support.

Solid sorbents are promising materials for CO₂ capture from air or flue gas.^{4–6} Here, we focus on CO₂ capture from air, where a solid sorbent typically functions in a temperature-dependent process.^{7,8} Capture takes place at low temperatures, and the sorbent is regenerated by heating, after which the desorbed CO₂ is collected for further use (carbon capture and utilization) or storage (carbon capture and storage). For an efficient process, it is essential that the sorbent has a high capture capacity and a fast capture rate. Desorption must take

Received: April 29, 2022

Revised: August 29, 2022

Accepted: August 29, 2022

Published: September 10, 2022

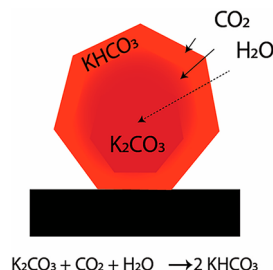


place at a low temperature to minimize the required energy input.

In general, CO_2 can be adsorbed on a solid via physisorption or chemisorption. In physisorption, the capture material binds CO_2 via weak van der Waals interactions. Materials such as microporous activated carbon can capture CO_2 from highly concentrated sources (10–20 vol %) such as flue gas via physisorption.^{9,10} In chemisorption, materials capture CO_2 via the formation of chemical bonds. Hence, they are more suitable to capture CO_2 from low-concentration sources (0.04 vol %) such as air.^{11,12} A broad range of chemisorption materials have been developed for CO_2 capture from air,^{11–14} such as metal–organic frameworks, immobilized amines, ionic liquids, and basic metal oxides.

Basic metal oxides and alkali metal carbonates such as calcium oxide (CaO), sodium carbonate (Na_2CO_3), and potassium carbonate (K_2CO_3) are promising solid sorbents.^{15–17} K_2CO_3 supported on carbon is especially promising for direct CO_2 capture from air¹⁸ because K_2CO_3 is thermally stable, is not toxic, is not corrosive, and is inexpensive. It reversibly reacts with CO_2 in the presence of water at room temperature (RT) to produce potassium bicarbonate (Scheme 1). Complete decomposition of the bicarbonate product can

Scheme 1. Presentation of a Multilayer Model: CO_2 and H_2O Diffuse into the Bulk K_2CO_3



be achieved at temperatures as low as 150 °C, which makes the energy requirements comparable to that of commercially applied amines in the liquid phase for CO_2 capture from flue gas.⁶

Unlike metal nanoparticles in catalysis, where only the particle outer layer adsorbs the reactants, the sorbent's active component, such as K_2CO_3 , potentially absorbs solutes such as CO_2 throughout the whole particle. Therefore, the sorption processes are best described by multilayer models in which CO_2 and H_2O diffuse into and react with the bulk K_2CO_3 to form a hydrate and/or bicarbonate (Scheme 1). Hence, the reaction with CO_2 (carbonation) involves two phases. First, K_2CO_3 on the outer layers reacts rapidly. Second, the bulk K_2CO_3 reacts in a slower phase that is limited by the diffusion of CO_2 and H_2O . That diffusion might be so slow that part of the K_2CO_3 in the core may never react.

According to Zhao et al.,¹⁹ internal diffusion is the rate-determining step during the carbonation of bulk K_2CO_3 . This (internal) diffusion limitation was also reported for other sorbents, such as $\text{Li}_2\text{CO}_3/\text{K}_2\text{CO}_3$ and CaO.^{20,21} Therefore, the size of the K_2CO_3 particles must be an important factor in determining the capacity and kinetics of the sorbent during CO_2 capture. It was suggested previously that nanoscale K_2CO_3 particles have a higher capacity for the sorbent;^{6,22–24} however, the size was not specified. The main reason for the lack of accurate size data is that no technique has been

established to analyze K_2CO_3 nanoparticles, especially when they are supported. Therefore, we investigated combinations of techniques to characterize supported alkali metal carbonates such as K_2CO_3 . Here, we aim to elucidate the size of K_2CO_3 particles that are supported on carbon.

We first prepared carbon-supported K_2CO_3 particles with different loadings, which were expected to result in different particle sizes. Next, conventional characterization techniques such as X-ray diffraction (XRD), scanning electron microscopy (SEM), and transmission electron microscopy (TEM) were used to establish the particle sizes but achieved limited success. Only TEM provided information about the K_2CO_3 particle size. Conversely, X-ray photoelectron spectroscopy (XPS) demonstrated a trend for particle size: The higher the loading was, the larger the K_2CO_3 particle size. Melting point depression measurements of K_2CO_3 , in combination with other techniques, ultimately resulted in the establishment of the average particle sizes in the different samples.

We studied K_2CO_3 /carbon sorbents for the capture of CO_2 from air in a fixed-bed flow-through reactor. We observed that the K_2CO_3 particle size critically affected the efficiency of the sorbent in CO_2 capture: The K_2CO_3 with the smallest size showed the fastest sorption and required the lowest temperature for CO_2 desorption. Hence, particle size directly affected the kinetics of the process as well as the required energy input. After the particle size effect was established, we unambiguously established the occurrence of diffusion limitations in the sorption of CO_2 over supported nanosized K_2CO_3 .

2. EXPERIMENTAL SECTION

2.1. Sample Preparation. Commercially available non-microporous carbon (KetjenBlack EC 600JD, AkzoNobel) was used to support K_2CO_3 . K_2CO_3 (Sigma-Aldrich, 99.995% trace metals basis) was deposited on the carbon by incipient wetness impregnation. In a typical preparation, the support (1 g) was dried under vacuum at 200 °C for 2 h. After cooling to RT, it was impregnated with an aqueous K_2CO_3 solution (1.7 mL) with an appropriate concentration to prepare 10, 25, and 50 wt % K_2CO_3 on the KetjenBlack support. The samples were aged at RT under vacuum for 30 min and then dried in a freeze drier at –80 °C under 0.1 mbar of vacuum for 18 h. The dried samples were collected and named according to their K_2CO_3 loading as KB10, KB25, and KB50. At least 4 different batches of each loading were prepared, characterized, and tested for CO_2 capture from air.

2.2. Characterization. Nitrogen physisorption measurements were performed at –196 °C (Micromeritics, TriStar II plus) to determine the BET surface area and porosity of the support and the sorbents.

XRD was carried out at the XPD beamline of the Brazilian Synchrotron Light Laboratory (LNLS) in Campinas, Brazil. The X-ray source was fixed at 8 keV ($\lambda = 1.5498 \text{ \AA}$). Powder samples were placed in an in situ high-temperature diffraction chamber (Anton Paar, XRK900) and heated in situ to 200 °C to eliminate the hydrate and bicarbonate forms. Crystallite sizes were determined from the peak broadening at $2\theta = 34.1^\circ$ using the Scherrer equation.

SEM was performed on an FEI Magellan 400 FESEM instrument equipped with an energy dispersive spectroscopy system from Oxford Instruments. For TEM imaging, either the dry powder samples or their diluted mixture with methanol were dispersed on TEM grids. TEM imaging was performed on a JEOL JEM-1400 Plus microscope operated at 120 kV.

XPS was performed on a Thermo Scientific K-alpha spectrometer equipped with a monochromated aluminum K α source with a photon energy of 1486.6 eV. Samples were handled in air and pressed in a copper powder sample holder without any further fixation. Sample charging was compensated by a flood gun during measurements. Binding energies were calibrated by setting the C 1s component belonging to graphitic sp² carbon to 284.5 eV. Quantitative analysis of the XPS data was performed using Casa XPS software (version 2.3.22PR1.0) based on high-resolution regional scans covering the K 2p and C 1s core levels in the binding energy range of 280–304 eV. For the KB10, KB25, and KB50 samples, the relative XPS intensity of potassium to carbon from the support, $(I_p/I_s)_{exp}$, was obtained by dividing the area of the K 2p peaks by the area of the C 1s sp² peak after correction for the relative sensitivity factors and the mean free path obtained from the included CasaXPS database (Scofield). The $(I_p/I_s)_{exp}$ value was used to estimate the relative size of the supported K₂CO₃ particles by using a quantitative XPS analysis model. A summary of the model and calculations is provided in the [Supporting Information](#).

Thermogravimetric analysis (TGA, Mettler-Toledo TGA/DSC1) was used to measure the melting point of the K₂CO₃ particles. The samples (~10–20 mg) were loaded in a 150 μ L alumina pan. The change in sample mass and heat flow were recorded during TGA under a flow of air (50 mL/min). Corrections for the buoyancy effect and background heat flow were performed by subtracting the data obtained from a blank experiment performed on the same pan prior to each experiment. The temperature and heat flow were calibrated with reference to a Au sample. The melting point was determined by following the endothermic heat flow at temperatures above 800 °C.

2.3. Performance in CO₂ Capture. CO₂ capture experiments were performed either via TGA or in a fixed-bed flow-through reactor. In a typical TGA experiment, the sorbent (K₂CO₃, KB10, KB25, or KB50, ~ 5 mg) was placed in a 40 μ L aluminum pan. The sorbent was pretreated from RT to 200 °C (ramp 10 °C/min) under flow of dry synthetic air (50 mL/min, zero CO₂ and H₂O concentrations) and kept at 200 °C for 30 min. Then, the sorbent was cooled to 60 °C to start the CO₂ capture experiment. The sorbent was exposed to a flow of air (50 mL/min, ~430 ppm of CO₂ and 60 ppm of H₂O) passing over the sample for 3 h, while the sorbent was kept at 60 °C. To vary the water concentration of the flow, the air was saturated with water vapor at different temperatures. The mass increase due to CO₂ and water uptake were then recorded.

Experiments in a fixed-bed flow-through reactor were performed in a Micromeritics AutoChem 2920 automated catalyst characterization system. The system was modified in house to involve an air flow with a constant and predetermined humidity. This was achieved by flowing the air constantly through a water vapor generator at a specified temperature. All water-containing lines were placed in a hot zone (110 °C) to stabilize the humidity of the flow.

In a typical experiment, the sorbent (KB10, KB25, or KB50, 50 mg) was placed in a U-shaped quartz plug flow reactor (internal diameter of 9 mm). The bed size was approximately 15 mm, and the gas hourly space velocity was approximately 120000 1/h. Under these conditions, there was no pressure drop over the reactor. Since the KetjenBlack support has a low mechanical stability, the samples were not sieved before use. The sorbent was pretreated from RT to 200 °C (ramp 10 °C/

min) under flow of dry He (50 mL/min) and kept at 200 °C for 30 min. Then, the sorbent was cooled to 60 °C to start the CO₂ capture experiment. The sorbent was exposed to a flow of air (50 mL/min, ~430 ppm of CO₂, 3 vol % H₂O) for a certain time (1, 2.5, 5, or 10 h), while the sorbent was kept at 60 °C. The outlet was analyzed every 1 s by a nondispersive infrared gas detector (LI-840A CO₂/H₂O gas analyzer, LI-COR) to record CO₂ and H₂O concentrations. CO₂ breakthrough curves during CO₂ capture from air were thus obtained. Furthermore, the CO₂ sorption capacity was obtained by dividing the total moles of CO₂ uptake by the dry amount of sorbent applied for each test. To calculate the efficiency of CO₂ uptake, the total moles of CO₂ uptake were divided by the corresponding moles of K₂CO₃ in each test. Here, a 1:1 stoichiometric mole ratio of CO₂ to K₂CO₃ was considered. Consecutively, CO₂ desorption upon heat treatment (10 °C/min up to 200 °C) under a flow of dry N₂ (50 mL/min) was performed.

3. RESULTS AND DISCUSSION

3.1. Structural Characterizations. To determine the textural properties of the samples and support, nitrogen adsorption–desorption isotherms for the KetjenBlack support, KB10, KB25, and KB50 were analyzed ([Supporting Information, Figure S1](#)). From the isotherms, the BET surface area, total pore volume, and micropore volume were obtained and are summarized in [Table 1](#). Upon increasing the K₂CO₃

Table 1. Summary of the Sample Pore Structures

sample	BET surface area (m ² /g sample)	total pore volume (mL/g) ^a	expected pore volume (mL/g) if pores are occupied by K ₂ CO ₃	micropore volume (mL/g sample)
KetjenBlack	1370	3.16	3.16	0.05
KB10	1210	2.83	2.86	0.04
KB25	950	2.10	2.45	0.03
KB50	700	1.51	1.37	0.02

^aTotal volume of pores smaller than ~400 nm width was measured at p/p^o of 0.99.

loading, the BET surface area and the total pore volume decreased. This decrease was expected since K₂CO₃ is not porous and the support is the only component with a porous structure.

We calculated the expected pore volume if all the pores (maximum size ~400 nm, measured at p/p^o of 0.99) were occupied by K₂CO₃ by considering the support pore volume, the K₂CO₃ loading of each sample, and the density of K₂CO₃ (2.43 g/cm³). These values are summarized in [Table 1](#). The total pore volume of the pores was only slightly smaller than the expected pore volume calculated for KB10 and KB25, indicating that the K₂CO₃ occupied pores in the support smaller than ~400 nm in the KB10 and KB25 sorbents. However, the total pore volume of the pores was slightly larger than the expected pore volume calculated for KB50, indicating that K₂CO₃ did not fully occupy the pores in KB50. One therefore may assume that the particle size is smaller than 400 nm for KB10 and KB25 and likely larger than 400 nm for KB50. However, determination of the particle size by the limitation of the pores is not explicit because the pores of the KetjenBlack support are not rigid but are prone to expansion and interconnected. Some pores can also be blocked upon deposition of the K₂CO₃, and the deviations are not large.

Hence, from the physisorption data, one can only assume that KB50 has larger size K_2CO_3 particles than the KB10 and KB25 sorbents.

XRD patterns of the samples (KB10, KB25, and KB50) before and after heating are shown in Figure 1. The

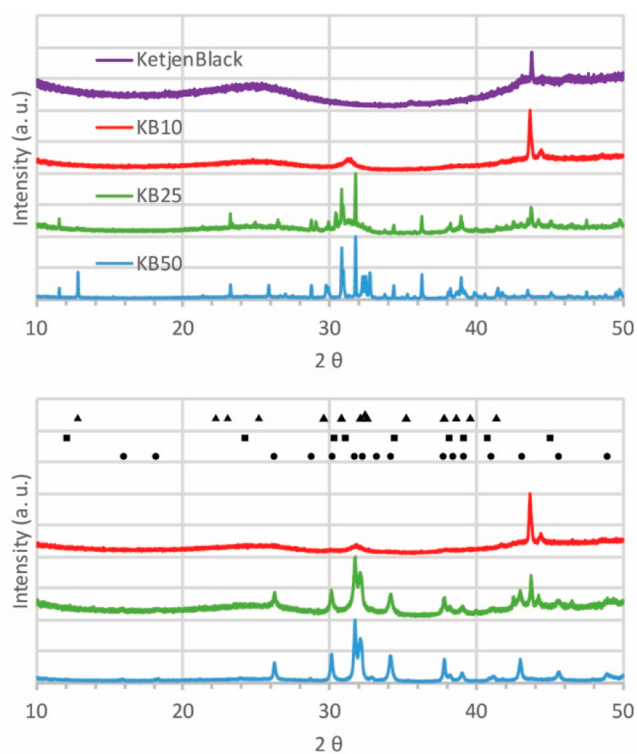


Figure 1. XRD patterns of KB10, KB25, and KB50 before (top) and after (bottom) the samples were heated in situ to 200 °C to eliminate hydrate and bicarbonate forms. References of K_2CO_3 (●), hydrate (▲), and bicarbonate (■) are shown on the patterns.

combination of different crystal phases, K_2CO_3 (reference PDF 87-0730), $KHCO_3$ (reference PDF 01-0976) and $K_2CO_3 \cdot 1.5H_2O$ (reference PDF 11-0655), is visible for the three sorbents before heating. Figure 1 shows that upon in situ heating, all the phases were converted to K_2CO_3 . From the broadening of the K_2CO_3 peak at 34.1°, crystallite sizes of 13, 30, and 36 nm for KB10, KB25, and KB50, respectively, were estimated. Notably, the crystallite size of bulk K_2CO_3 was approximately 56 nm, depending on its source and preparation. Therefore, the crystallite sizes of these samples, bulk and supported K_2CO_3 , are not largely different; however, their particle sizes can still be very different and larger than the crystallite sizes (see below (Figure 2) for TEM where the

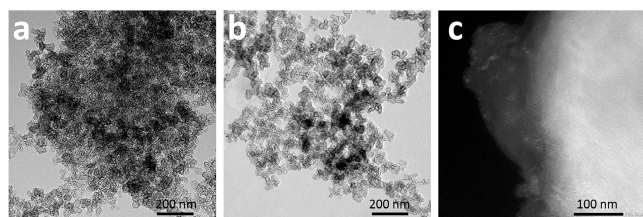


Figure 2. TEM images of KetjenBlack (a) and KB50 (b). Dark-field TEM image of K_2CO_3 on a carbon support that shows the presence of a crystalline structure (c).

smallest particle size observed was 140 nm). It is likely that the particle size is larger than the crystallite size, and every particle contains crystallites of different domains in the range of 10–40 nm. Hence, XRD provides an average crystallite size but is not useful to estimate particle sizes.

Next, different techniques were applied to visualize the K_2CO_3 particles directly in an attempt to determine their particle sizes. SEM coupled with EDX elemental mapping showed the presence of K_2CO_3 on the carbon support (Figure S2). Some very large particles of approximately 18 μm as well as some particles of approximately 0.5 μm were distinguishable in the images. However, nanoparticles were not observed by SEM, although their presence could be inferred from the fact that the elemental mapping indicated the presence of K even when no particles were visible. Extraction of an average particle size was therefore not possible.

TEM images of the carbon support and the K_2CO_3 /carbon are shown in Figure 2a,b. The images do not differentiate K_2CO_3 from the carbon support, as the K_2CO_3 and the carbon support have very similar electron densities; hence, they display little contrast in bright-field TEM. Dark-field TEM images of K_2CO_3 on the carbon support (Figure 2c) showed some crystalline K_2CO_3 structures; however, this technique was not able to clearly distinguish K_2CO_3 particles to measure their size.

In an attempt to visualize the K_2CO_3 particles by TEM without interference from the carbon support, we removed the carbon by calcining it at 700 °C under air. Since solid K_2CO_3 is thermally stable up to its melting point at 895 °C, particles of K_2CO_3 were assumed to be intact. TEM imaging (Figure 3)

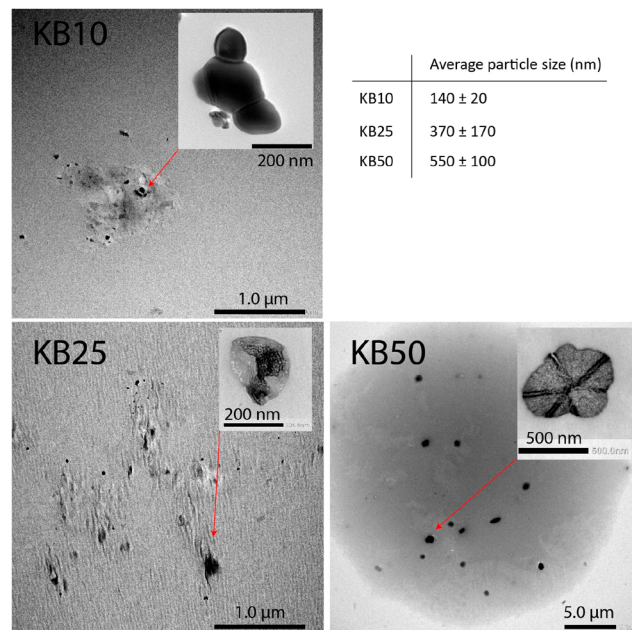


Figure 3. TEM images of KB10, KB25, and KB50 after burning the carbon support in air under TGA conditions.

clearly showed particles of K_2CO_3 containing different crystalline facets. Approximately 3–10 particles of K_2CO_3 could be isolated and measured. Average particle sizes of 140, 370, and 550 nm were estimated for the KB10, KB25, and KB50 samples, respectively, though with a large standard

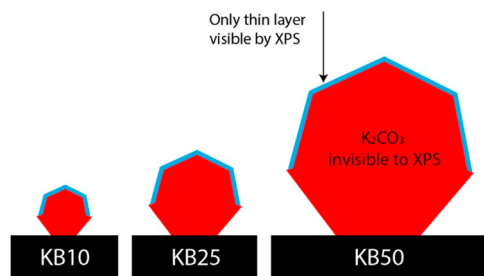
deviation. Hence, TEM imaging suggested a trend for particle size: KB10 < KB25 < KB50.

During imaging, we noticed that K_2CO_3 is very sensitive to the electron beam and that the particles changed as soon as they were exposed. TEM images of one K_2CO_3 particle, captured over time, show rapid changes in K_2CO_3 under the beam (Figure S3). Moreover, the samples seemed to be slightly inhomogeneous. Hence, larger particles could be overlooked during TEM imaging. Consequently, the average particle size is subject to error, although some of the K_2CO_3 particles were visualized by TEM. Therefore, there is a need for a bulk technique to determine the average size of the particles. Please note that these supports have mesopores while the supports used in our previous study on support effects has micropores.²⁵ We did not observe that limitation gas phase diffusion effects in those microporous supports; thus, we do not expect them to happen in the current mesoporous support

In the following, we estimate the K_2CO_3 particle sizes for KB10, KB25, and KB50 via a quantitative XPS analysis model developed by Kerkhof and Moulijn.²⁶ A summary of the model, the assumptions used to simplify the model, and the adaptations applied to make it suitable for the case of K_2CO_3 supported on carbon are explained in the Supporting Information. In summary, the model quantitatively correlates the signal ratio between an element of the supported metal/metal oxide and an element of the support to the dispersion of the metal/metal oxide on that support. Since smaller particles have higher dispersion and XPS is a surface-sensitive technique, a higher signal ratio for metal(oxide)/support is an indicator of smaller particles. Here, we used the K/C ratio to obtain a K_2CO_3 particle size. Particle sizes of 3, 7, and 30 nm were estimated by applying the model to KB10, KB25, and KB50, respectively.

The sizes determined by the Kerkhof–Moulijn method are in a different range than expected based on the TEM images of K_2CO_3 particles (3–30 nm vs 100–550 nm). This discrepancy is because the particles are too large for the XPS method; thus, the majority of K_2CO_3 is invisible by XPS. Scheme 2 illustrates

Scheme 2. Presentation of K_2CO_3 Particles with Different Sizes and the Portion That Is Visible by XPS



the portion of K_2CO_3 particles that are visible by XPS when particles are large and have different sizes. Notably, for simplicity, the particles were considered spheres in the calculation, while they likely have crystalline structures with crystallite faces. In any case, the XPS penetration depth is approximately 3–5 times greater than the inelastic mean free path of the electrons in a medium. The inelastic mean free path of a K 2p electron in K_2CO_3 excited by Al $K\alpha$ radiation is 3.3 nm.²⁷ Hence, XPS detected only the skin of the particles with a size no larger than 15 nm (more details on the qualitative XPS can be found in Figures S4 and S5 and Table S1). This skin

size is equal for all particles larger than 15 nm. Nevertheless, for smaller particles compared to larger ones, overall, a greater volume of K_2CO_3 is visible by XPS. This finding is interpreted as a smaller particle size. Therefore, XPS quantification cannot directly provide the particle sizes but can rank the samples with different K_2CO_3 particle sizes based on their volume visible by XPS.

If the model suggests particle sizes of 3, 7, and 30 nm for K_2CO_3 in different samples, the visible particle size ratio would be, in order, 1 to 2.4 to 10. The visible volume of the particles can be estimated by raising this particle size ratio to a power of three. Hence, the corresponding volume detected by XPS is 1:14:1070 for KB10, KB25, and KB50. Now, we have a ratio for visible volume in XPS for different particles, which corresponds to the particles' skin volume that is visible by XPS. One can translate the ratio for visible volume in XPS to a relative particle surface area. This process is possible since the skin size is the same for all the samples (~15 nm). Hence, the relative surface area of the particles would also be 1:14:1070. We need to extract a ratio for particle size. Hence, a relative particle size was estimated by calculating the square root of this relative surface area: 1:4:30. Accordingly, KB25 is four times larger than KB10, and KB50 is 30 times larger than KB10, although one may consider this approach very speculative.

We further evaluated the melting point depression of the samples. Melting point depression is the phenomenon in which the melting point of a nanoscale material, i.e., metal, metal oxide and salts, decreases upon reduction in the size of the material.²⁸ Therefore, melting point depression does provide information on particle size. Melting point depression follows the Gibbs–Thomson relation:²⁹

$$T'_m = T_m \left(1 - \frac{4\gamma_{sl}V_m}{R\Delta_{fus}H} \right)$$

where T'_m is the melting temperature of the nanoparticle, T_m is the bulk melting temperature, γ_{sl} is the solid/liquid surface tension equal to 0.1693 J/m² for K_2CO_3 ,^{30,31} V_m is its molar volume equal to 56.87×10^{-6} m³/mol, R is the particle diameter in m, and $\Delta_{fus}H$ is the K_2CO_3 melting molar enthalpy equal to 27.60×10^3 J/mol.

The melting point of the K_2CO_3 particles was measured by following the heat flow during TGA under the flow of air (Figure 4). Please note that these experiments had to be performed in air i.e. while burning the carbon. When the experiments were performed in nitrogen (Figures S6 and S7), no unambiguous heat effect was observed most likely because the carbon reacts (is oxidized) with K_2CO_3 around its melting point. Figure 4a shows that carbon is burned at temperatures of approximately 700 °C. The mass loss scaled only with the carbon content of the samples; hence, K_2CO_3 did not form volatile compounds. Figure 4b shows that by increasing the temperature from 860 to 920 °C, heat consumption due to melting of the K_2CO_3 occurred. Figure 4c shows the evolution of heat flow with temperature in the range of 860–920 °C. Bulk K_2CO_3 melts at 895 °C. The K_2CO_3 in the KB50, KB25, and KB10 samples melted in order at lower temperatures: 894, 888, and 881 °C with ± 1 °C variation from triplicate experiments. This result confirms the trend for particle size: KB10 < KB25 < KB50.

By applying the Gibbs–Thomson equation, we estimated a size of 120 ± 20 nm for KB10 and a size of 230 ± 70 nm for KB25. The size for the KB50 sample was estimated to be in the

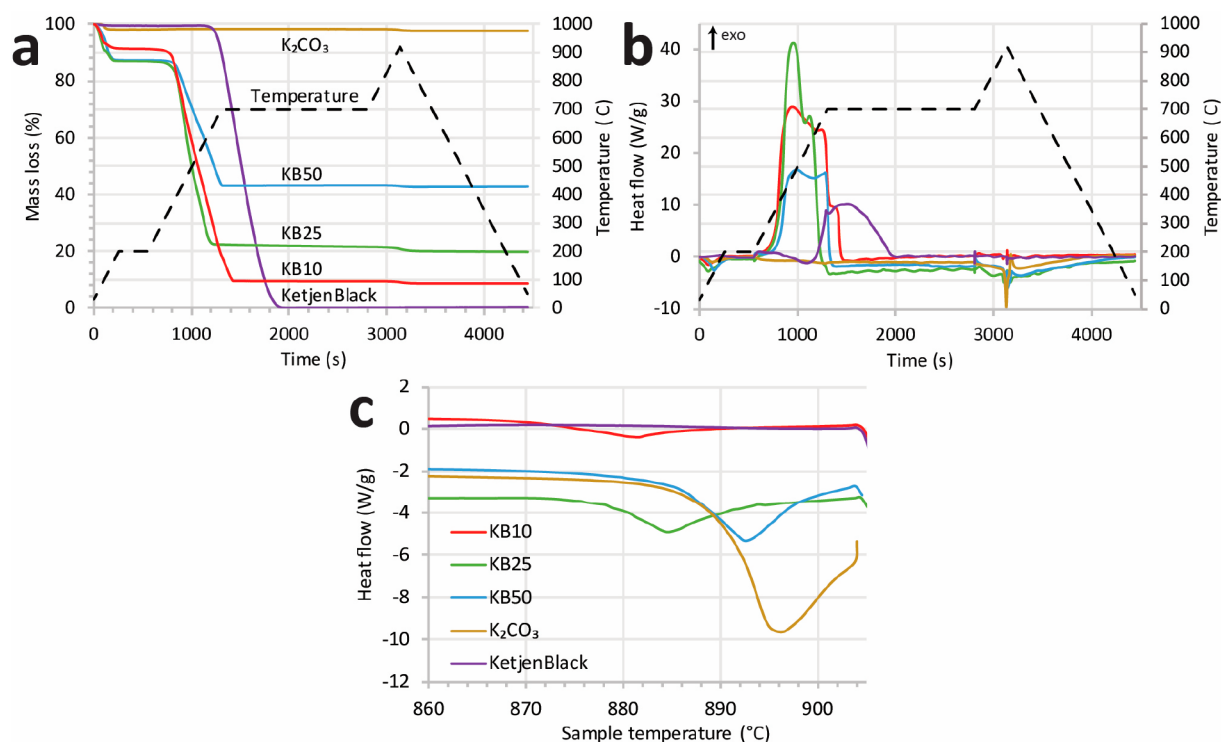


Figure 4. Evolution of the relative mass (a) and heat flow (b and c) with the temperature on KetjenBlack support, bulk K_2CO_3 , KB10, KB25, and KB50 samples. The samples were heated to 920 $^{\circ}C$ under flow of synthetic air (50 mL/min, zero CO_2).

size range of 600–1600 nm, which is similar to the bulk size of approximately 1.5 μm . Though the trend in particle size is clear from the melting point, the absolute particle size has a relatively large error margin because the ± 1 $^{\circ}C$ variation in melting point for these samples lies in a region where a minor change in melting point leads to a considerable change in particle diameter (Figure S8). Nevertheless, from the Gibbs–Thomson equation, one can accurately extract the ratio of particle size for different samples as below:

$$\frac{R_{KB25}}{R_{KB10}} = \frac{T_m - T_m^{KB10}}{T_m - T_m^{KB25}}$$

According to the ratio obtained from the melting point depression, KB25 is twice as large as KB10, and KB50 is 14 times larger than KB10.

In summary, TEM, after the carbon support was eliminated, was used to visualize K_2CO_3 particles with sizes of 140, 370, 550 nm for KB10, KB25, and KB50, respectively. XPS speculatively suggested a size ratio of 1:4:30, while melting point depression suggested a size ratio of 1:2:14. Melting point depression determined average particle sizes of 120, 230, and ~ 1000 nm for KB10, KB25, and KB50, respectively. There are differences in the particle sizes estimated by different techniques. Nevertheless, the trend is clear: The higher the loading is, the larger the K_2CO_3 particle size.

3.2. Performance in CO_2 Capture from Air. TGA was used to get an initial idea of the kinetics of the sorbents for CO_2 capture, as TGA is an often applied technique for this. Please note that our TGA results (and earlier reported results) might suffer from mass transfer limitations. Figure 5 shows the increase in the mass of the sorbents upon exposure to air that contains 440 ppm of CO_2 and 60 ppm water. A fast initial mass increase occurred for KB10 and KB25. For KB10, the mass

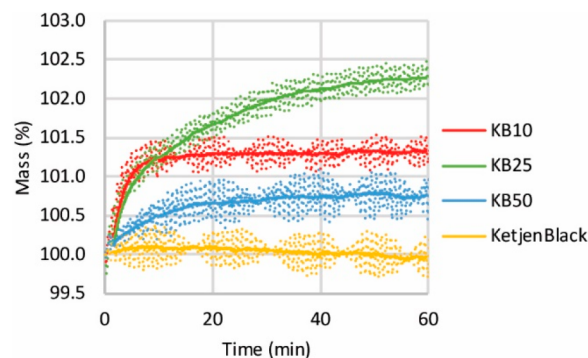


Figure 5. Mass increase due to exposure of the KetjenBlack support, KB10, KB25, and KB50 samples to air (approximately 2 mg of sample), pretreated at 200 $^{\circ}C$ under 150 mL/min flow of dry synthetic air (no CO_2), sorption at 60 $^{\circ}C$ under 150 mL/min flow of air (containing 440 ppm of CO_2 and 60 ppm of H_2O).

increase leveled off to zero, while for KB25, a slow steady mass increase occurred. For KB50, the initial mass increase was slow and leveled off to a very low value.

In these experiments, a low amount of water (60 ppm) was applied to avoid preferential water uptake compared to CO_2 uptake, which would lead to miscalculation of the capacity of the sorbents in capturing CO_2 . We observed that increasing the water content of the flow led to an increase in the total uptake of the sorbents (Figure S9). It is not trivial to attribute the total mass increase to only CO_2 uptake, as the formation of a hydrate ($K_2CO_3 \cdot 1.5H_2O$) in addition to the bicarbonate ($KHCO_3$) is quite possible and likely preferred. It was reported earlier by Jayakumar et al.³² that attributing the mass increase in a typical TGA to CO_2 capture introduces error in the calculation of the sorbent capacity. It is possible

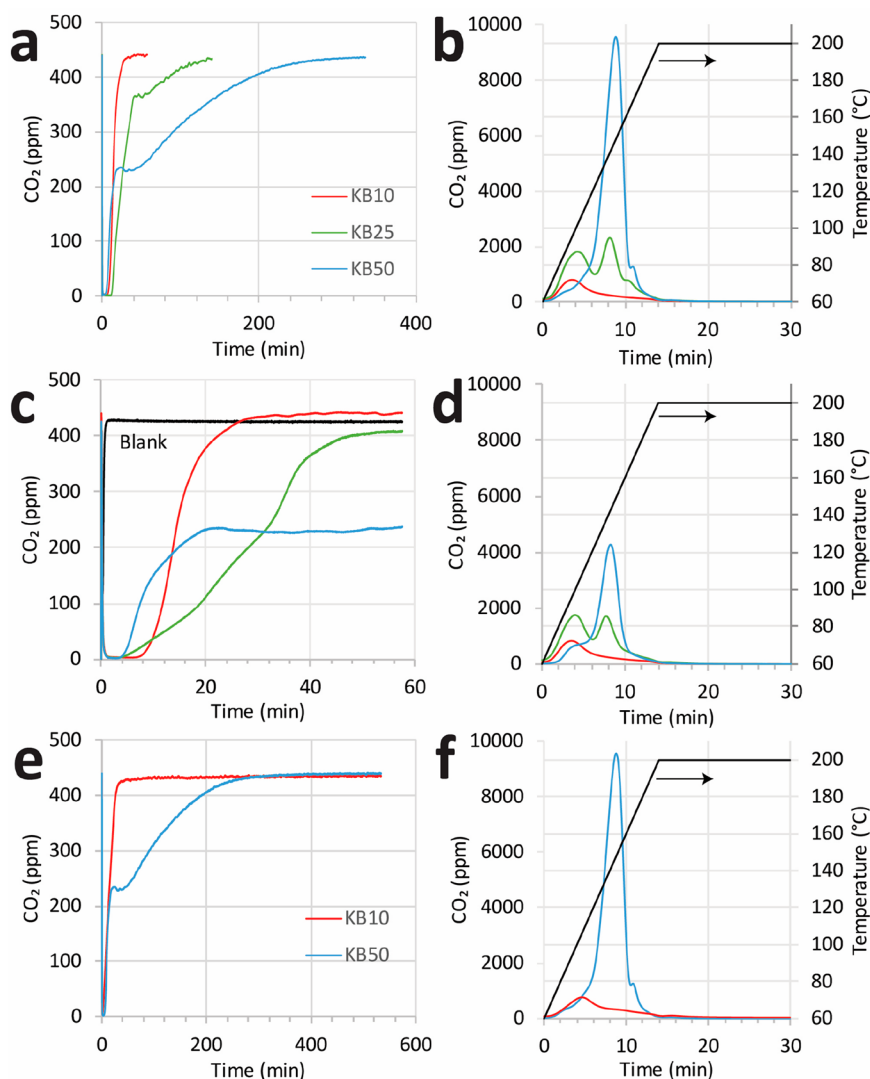


Figure 6. CO₂ breakthrough curves during CO₂ capture from air during 5 h (a), 1 h (c), and 10 h (e) of capture. The air passed through different sorbents (KB10, KB25, and KB50, 50 mg), pretreatment RT to 200 °C: 10 °C/min, dwell time of 30 min under flow of dry He (50 mL/min), sorption at 60 °C until reaching the air CO₂ concentration, flow of air (50 mL/min, 430 ppm of CO₂), water content: 3 vol % (vapor generated at 25 °C). Consecutive decarbonation upon heat treatment (10 °C/min up to 200 °C) under flow of dry N₂ (50 mL/min) after 5 h (b), 1 h (d), and 10 h (f) of capture. The CO₂ concentration was measured by a nondispersive infrared gas detector.

Table 2. CO₂ Sorption Capacity of the Samples^a

sample	total CO ₂ uptake (mmol CO ₂ /g sorbent)	total CO ₂ uptake (mol CO ₂ /mol K ₂ CO ₃)	capture time (min)	CO ₂ uptake rate (mol CO ₂ /h-mol K ₂ CO ₃)	CO ₂ uptake after 20 min (mol CO ₂ /mol K ₂ CO ₃)	CO ₂ uptake after 1 h (mol CO ₂ /mol K ₂ CO ₃)	CO ₂ uptake after 10 h (mol CO ₂ /mol K ₂ CO ₃)
KB10	0.3	0.5	40	0.7	0.5	0.5	0.5
KB25	0.7	0.4	140	0.2	0.2	0.4	–
KB50	1.4	0.4	335	0.1	0.1	0.2	0.4

^aCO₂ uptake is normalized to the dry amount of the sample.

that the presence of water and/or CO₂ at specific concentrations affects the diffusion of the other component as well. Hence, extracting accurate CO₂ uptake values from TGA data is difficult due to interfering water uptake and/or a low water concentration.

Earlier reports on K₂CO₃ for CO₂ capture were mostly performed via TGA, where unsupported K₂CO₃ was exposed to a flow containing CO₂.^{19,32–35} Therefore, we continue to compare the sorbents in a fixed-bed flow-through reactor in which the changes in CO₂ concentration are directly measured.

Figure 6a shows the breakthrough of the sorbents in CO₂ capture. KB10 showed fast sorption and was saturated during the first 20 min of sorption. KB25, however, after an initial fast uptake, continued to capture CO₂ during 2 h of sorption. KB50, after an initial fast uptake, showed slow and steady uptake during 5 h of sorption. The general trend agrees with the data obtained by TGA. Table 2 summarizes the CO₂ uptake of the sorbents over time. The highest K₂CO₃ loading (KB50 compared with KB25 and KB10) led to the highest total CO₂ uptake per gram of sorbent in 5 h of capture (1.4

mmol CO₂/g sorbent). The sorbent with the lowest loading but the smallest K₂CO₃ particle size (120 nm for KB10 compared to 230 and 1000 nm for KB25 and KB50) achieved the highest efficiency of CO₂ capture per amount of K₂CO₃ in the shortest time.

By examining the breakthrough curves after 1 h of sorption for all three sorbents (Figure 6c), one can see that KB10 with the smallest K₂CO₃ particle size showed the fastest sorption compared to KB50 with the largest K₂CO₃ size. The CO₂ uptake rate normalized per mol K₂CO₃ was 0.7 mol CO₂/h for KB10 and 0.1 mol CO₂/h for KB50. This finding confirms that the sorption follows an initial fast sorption followed by a slower process that occurred only for K₂CO₃ with a larger particle size, while for K₂CO₃ with a smaller size, the accessible K₂CO₃ immediately contributed to the reaction.

Figure 6b shows the consecutive desorption of CO₂ upon heating the sorbent to 200 °C. Desorption occurred at 100 °C for KB10. The desorption occurred at a higher temperature for KB50 (140 °C). KB25, with an intermediate size, showed two desorption peaks at the temperatures at which desorption occurred for KB10 and KB50. Notably, the decarbonation temperatures for KB10, KB25, and KB50 in the flow unit match the decarbonation temperatures during TGA (Figure S10). The desorption peak height is considerably higher for KB50 than for KB25 and KB10. This shows that KB50 definitely captured more CO₂ than KB10 and KB25, although at the expense of exposure to air for a longer time and desorption that occurred at higher temperatures.

Consecutive desorption of CO₂ after 1 h of sorption (Figure 6d) resulted in a lower CO₂ uptake for KB50 compared to sorption in 5 h. In this case, there was no difference between KB10 and KB25 after sorption for a longer time. This result suggests that diffusion of CO₂ into K₂CO₃ in the KB50 sample with a larger size was limited, since by exposing the KB50 sample to the air flow for a longer time, CO₂ uptake was increased.

Figure 6e,f shows the CO₂ breakthrough after 10 h of capture and consecutive desorption of CO₂ for the KB50 and KB10 sorbents. The figures show that by exposing the KB10 to air for a longer time, CO₂ capture was not enhanced. Hence, in all three sorbents, regardless of the capture time, at least half of the K₂CO₃ remained unreactive. This means that for K₂CO₃ with different sizes, diffusion of CO₂ and water into K₂CO₃ is limited to a certain penetration depth, and further diffusion is not possible. Nasiman and Kanoh²³ reported CO₂ capture from air under TGA conditions by 60 wt % K₂CO₃ in K₂CO₃–carbon nanocomposites. From the XRD peak broadening, they estimated a size of approximately 20 nm for K₂CO₃ particles. From the provided data, we calculated an efficiency of ~0.8 mol CO₂/mol K₂CO₃ for that sorbent. These data indicate that with smaller particles, the efficient use of K₂CO₃ in a certain period is enhanced. Furthermore, part of the K₂CO₃ in the core may never react.

3.3. Evaluation of the Diffusion Phenomena. We estimated the CO₂ penetration depth over time for the KB10, KB25 and KB50 sorbents by considering the estimated size of the K₂CO₃ particles obtained by melting point depression and considering the capacity of the sorbents for capturing CO₂ per mole of the K₂CO₃ over time. Every mole of reacted K₂CO₃ can be related to an accessible volume in the outer layers. The calculated CO₂ penetration depths over time for the three sorbents are summarized in Table 3. The penetration depths for KB10 and KB25 are 10 and 20 nm, respectively; however,

Table 3. Calculated CO₂ Penetration Depth over Time Based on K₂CO₃ Particle Size and Capacity of the Samples in CO₂ Capture

	time of capture (min)	efficiency in CO ₂ capture (mol CO ₂ /mol K ₂ CO ₃)	particle diameter (nm)	estimated penetration depth (nm)
KB10	40	0.5	120	10
KB25	140	0.4	230	20
KB50	335	0.4	1000	80

these values are as high as 80 nm for the KB50 samples. Hence, CO₂ and H₂O somehow diffused more into the bulk K₂CO₃ in the KB50 sample. Furthermore, one may assume that the CO₂ and H₂O diffusion for the KB50 with larger K₂CO₃ particles follows a different mechanism than that followed by the KB10 sample with smaller K₂CO₃ particles. Different possible diffusion mechanisms are discussed below.

Diffusion of CO₂ and H₂O gases into K₂CO₃ may follow specific pathways such as microstructures and/or defects that are developed as K₂CO₃ particles grow. Generally, the diffusion of ions in solids is dependent on the presence of defects.³⁶ It is possible that microstructures and/or defects are developed more as the K₂CO₃ particles grow larger, e.g., KB50. The diffusion rate for KB50 was calculated as 3.8 × 10⁻⁷ cm/min, which is in the range for gas transport in porous material.³⁷ This suggests that diffusion via microstructures and/or defects contributed at least in the KB50 sample. Please note that the results up to now indicate that KB50 particles consist of aggregates. This might be the specific microstructure of the KB50 sample which influences its sorption behavior; further study is needed to investigate the exact role of particle size on that.

Moreover, diffusion of CO₂ and H₂O gases into K₂CO₃ may also follow via an ion conductivity mechanism in which the layer of produced KHCO₃ acts like a pool of CO₂ and H₂O that allows CO₂ and H₂O to penetrate into an outer layer of the pool, while inner CO₂ and H₂O molecules migrate into the K₂CO₃ core. When the KHCO₃ layer is thickened, the diffusion length is longer; hence, the diffusion of CO₂ and H₂O into the core becomes slower according to Fick's first law of diffusion.³⁸ It has been suggested earlier by Luo et al.³⁹ that the production of KHCO₃ can hinder further diffusion of CO₂ and H₂O into bulk K₂CO₃. Hence, this diffusion mechanism occurs gradually upon formation of additional KHCO₃ so that, in practice, part of the K₂CO₃ in the core may never react. Based on our observation of all three sorbents, regardless of the capture time, at least half of the K₂CO₃ remained unreactive. This observation suggests that ion conductivity is an involved mechanism in the diffusion of CO₂ and H₂O gases into K₂CO₃.

To further evaluate the diffusion mechanism, we evaluated the decarbonation steps to determine whether they are activated processes. By increasing the heating rate upon decarbonation, one would expect a shift to higher temperatures if the decarbonation is an activated process.⁴⁰ Figure 7 shows the desorption of CO₂ from the KB25 sorbent upon heat treatment. Note that KB25 with an intermediate size showed the dual desorption properties of KB10 and KB50, which means that desorption occurred partially at 100 °C and partially at 140 °C. In all three experiments, the CO₂ uptake was the same, and upon heat treatment, the captured CO₂ was fully desorbed. As the heating rate was increased from 5 to 20 °C/min, the peaks due to decarbonation were shifted to higher temperatures. This means that both decarbonation steps were

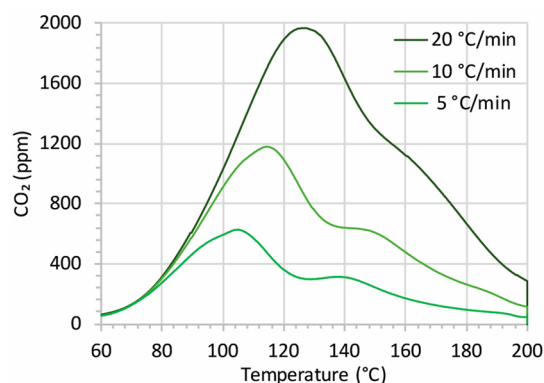


Figure 7. Decarbonation upon heat treatment with different heating rates up to 200 °C under flow of dry N₂ (50 mL/min) after a 1 h typical capture experiment. The sorbent was KB25.

activated processes. The apparent activation energies for both steps were calculated to be 69 and 93 kJ/mol. The basis of the calculation was the Redhead analysis,⁴⁰ and details of the calculation are explained in the [Supporting Information](#).

In the literature, a shrinking core model was used to describe the kinetics of the K₂CO₃ carbonation reaction.¹⁹ According to this model, the reaction takes place only on a surface, dividing the unreacted core from the product shell in one particle, while the core shrinks as the reaction continues. The shrinking core model is valid when the reaction is limited by diffusion of the gases into the core rather than being limited by the reaction kinetics.⁴¹ According to this model and on the basis of experimental data of CO₂ capture from flue gas at temperatures of 55–80 °C and a CO₂ pressure of 0.1 MPa, Zhao et al.¹⁹ calculated an apparent activation energy of 33.4 kJ/mol for the K₂CO₃ carbonation reaction and 99.1 kJ/mol for the diffusion-limited step of the reaction. One can assume that the diffusion-limited step of the carbonation and decarbonation reactions must match. The activation energy of 99.1 kJ/mol for the diffusion-limited step of the reaction in Zhao's work is close to the activation energy of 93 kJ/mol that we obtained for the second step of decarbonation. These numbers are rather high and might reflect a combination of breaking of chemical bonds and diffusion.⁴¹ The second step of decarbonation is perhaps fully diffusion limited, as it is more pronounced for KB50 with a larger size of K₂CO₃ than for KB10 with a smaller size of K₂CO₃. One may note the difference in the reaction conditions of our experiments and the work of Zhao et al.¹⁹ and note that the experimental data obtained by TGA must be treated carefully due to interfering water effects and possible hydration/dehydration reactions as pointed out by Jayakumar et al.³² Nevertheless, we agree with the literature that the K₂CO₃ carbonation reaction is diffusion limited, and we suggest a value of 93 kJ/mol for the diffusion-limited step of the carbonation reaction.

Although KB50 with higher K₂CO₃ loading showed higher capacity of CO₂ capture, KB10 with smaller K₂CO₃ particles showed higher efficiency of capture. CO₂ penetrated farther into larger particles but at the expense of longer capture times. This second layer of captured CO₂ demanded more energy to be desorbed as well. Therefore, the sorbent preparation method must fulfill the criteria of a high loading of K₂CO₃ and a small particle size. This is an important consideration for the development of supported solid sorbents, and it is being actively researched in our group. We note here that this

reasoning does match with our observations; however, many questions regarding the mechanism remain open like the exact nature of the phases formed during sorption and desorption and the exact kinetics and role of water on that. Another very relevant question is to what extent do all K₂CO₃ participate in the sorption process.^{42,43} However, here we focused on the role of particle size and show that there is a particle size effect. More research is needed to fully understand the particle size effect.

4. CONCLUSION

In summary, we prepared a series of carbon-supported K₂CO₃ particles with different sizes by varying the K₂CO₃ loading. Conventional techniques were not able to decisively determine the average K₂CO₃ particle sizes, but melting point depression of the K₂CO₃ particles could be used to estimate an average particle size for the three prepared sorbents. This is the first time that the size of supported K₂CO₃ nanoparticles has been quantitatively determined and related to performance data of CO₂ sorption. We further studied the sorbents for the capture of CO₂ from air in an industrially scalable flow-through setting. The K₂CO₃ with the smallest size showed the fastest sorption. The sorbent with the highest K₂CO₃ loading showed the highest uptake, though at the expense of a longer time. In this sorbent, with the highest loading and largest K₂CO₃ particle size, CO₂ penetrated farther into the bulk of the particle; however, the internal layers of the captured CO₂ were desorbed at a higher temperature. We confirmed that desorption is an activated process. The apparent activation energy for the diffusion-limited desorption step was calculated to be 93 kJ/mol. Therefore, the size of the K₂CO₃ particles is an important factor in the design of this type of solid sorbents. K₂CO₃ particle size critically affected the efficiency of the sorbent in CO₂ capture relative to the amount of active component being active for sorption, and it directly affects the kinetics of the process as well as the sorbent capacity and energy input for the desorption process. Therefore, we conclude that an ideal sorbent based on supported K₂CO₃ must have a high loading of K₂CO₃ and a small particle size. This is an important consideration for the development of suitable sorbents for CO₂ capture from air.

■ ASSOCIATED CONTENT

SI Supporting Information

The Supporting Information is available free of charge at <https://pubs.acs.org/doi/10.1021/acs.iecr.2c01508>.

Nitrogen isotherms of the samples, SEM images and EDX mapping of KB50 and KB25, TEM images of one K₂CO₃ particle exposed to beam captured over time, XPS spectra of the samples and quantitative analysis of XPS data including summarized variables applied in the model and the model prediction for K₂CO₃ particle sizes, TGA for analysis of melting point depression under nitrogen, description of thermodynamically stable components under nitrogen at high temperatures, the relation of melting point to the K₂CO₃ particle size according to the Gibbs–Thomson equation, TGA upon exposure to wet air, TGA during decarbonation, details of the calculation of apparent activation energy for decarbonation steps including variables of the Redhead analysis and Arrhenius plot of the decarbonation steps (PDF)

AUTHOR INFORMATION

Corresponding Authors

Johannes Hendrik Bitter – *Biobased Chemistry and Technology, Wageningen University, 6700AA Wageningen, The Netherlands*; orcid.org/0000-0002-4273-9968;
Email: harry.bitter@wur.nl

Nazila Masoud – *Biobased Chemistry and Technology, Wageningen University, 6700AA Wageningen, The Netherlands*; orcid.org/0000-0001-7216-4133;
Email: nazila.masoud@wur.nl

Authors

Victorien Clement – *Biobased Chemistry and Technology, Wageningen University, 6700AA Wageningen, The Netherlands*

Tomas van Haasterecht – *Biobased Chemistry and Technology, Wageningen University, 6700AA Wageningen, The Netherlands*

Marlene Führer – *Biobased Chemistry and Technology, Wageningen University, 6700AA Wageningen, The Netherlands*

Jan P. Hofmann – *Laboratory for Inorganic Materials and Catalysis, Department of Chemical Engineering and Chemistry, Eindhoven University of Technology, 5600MB Eindhoven, The Netherlands*; *Surface Science Laboratory, Department of Materials and Earth Sciences, Technical University of Darmstadt, 64287 Darmstadt, Germany*;
orcid.org/0000-0002-5765-1096

Complete contact information is available at:
<https://pubs.acs.org/10.1021/acs.iecr.2c01508>

Notes

The authors declare no competing financial interest.

ACKNOWLEDGMENTS

We gratefully acknowledge Roxani Chatzipanagiotou for SEM imaging, Lakshminarasimhan Sridharan for dynamic light scattering measurements, Xiaofeng Wu (Eindhoven University of Technology) for performing XPS measurements, Cristiane Barbieri Rodella (Brazilian Synchrotron Light Laboratory) for providing a beamtime opportunity, and Carlos Cabrera Rodriguez, Lars Kiewidt, Antecy and Bronswerk Heat Transfer for the contribution of the CAIR in the CO₂ capture from air project. We are grateful to the European Regional Development Fund for the overall funding of the project (project number: PROJ-00675).

REFERENCES

- (1) Ishida, T.; Murayama, T.; Taketoshi, A.; Haruta, M. Importance of Size and Contact Structure of Gold Nanoparticles for the Genesis of Unique Catalytic Processes. *Chem. Rev.* **2020**, *120*, 464–525.
- (2) Bezemer, G. L.; Bitter, J. H.; Kuipers, H. P.; Oosterbeek, H.; Holewijn, J. E.; Xu, X.; Kapteijn, F.; van Dillen, A. J.; de Jong, K. P. Cobalt Particle Size Effects in the Fischer–Tropsch Reaction Studied with Carbon Nanofiber Supported Catalysts. *J. Am. Chem. Soc.* **2006**, *128*, 3956–3964.
- (3) Van Den Reijen, J. E.; Kanungo, S.; Welling, T. A. J.; Versluijs-Helder, M.; Nijhuis, T. A.; De Jong, K. P.; De Jongh, P. E. Preparation and Particle Size Effects of Ag/ α -Al₂O₃ Catalysts for Ethylene Epoxidation. *J. Catal.* **2017**, *356*, 65–74.
- (4) Mac Dowell, N.; Fennell, P. S.; Shah, N.; Maitland, G. C. The Role of CO₂ Capture and Utilization in Mitigating Climate Change. *Nat. Clim. Change* **2017**, *7*, 243–249.
- (5) Sanz-Perez, E. S.; Murdock, C. R.; Didas, S. A.; Jones, C. W. Direct Capture of CO₂ from Ambient Air. *Chem. Rev.* **2016**, *116*, 11840–11876.
- (6) Meis, N. N. A. H.; Frey, A. M.; Bitter, J. H.; de Jong, K. P. Carbon Nanofiber-Supported K₂CO₃ as an Efficient Low-Temperature Regenerable CO₂ Sorbent for Post-Combustion Capture. *Ind. Eng. Chem. Res.* **2013**, *52*, 12812–12818.
- (7) Fasihi, M.; Efimova, O.; Breyer, C. Techno-Economic Assessment of CO₂ Direct Air Capture Plants. *J. Cleaner Prod.* **2019**, *224*, 957–980.
- (8) Krekel, D.; Samsun, R. C.; Peters, R.; Stolten, D. The Separation of CO₂ from Ambient Air – A Techno-Economic Assessment. *Appl. Energy* **2018**, *218*, 361–381.
- (9) D'Alessandro, D. M.; Smit, B.; Long, J. R. Carbon Dioxide Capture: Prospects for New Materials. *Angew. Chem., Int. Ed.* **2010**, *49*, 6058–6082.
- (10) Oschatz, M.; Antonietti, M. A Search for Selectivity to Enable CO₂ Capture with Porous Adsorbents. *Energy Environ. Sci.* **2018**, *11*, 57–70.
- (11) Shi, X.; Xiao, H.; Azarabadi, H.; Song, J.; Wu, X.; Chen, X.; Lackner, K. S. Sorbents for the Direct Capture of CO₂ from Ambient Air. *Angew. Chem., Int. Ed.* **2020**, *59*, 6984–7006.
- (12) Goeppert, A.; Czaun, M.; Surya Prakash, G. K.; Olah, G. A. Air as the Renewable Carbon Source of the Future: an Overview of CO₂ Capture from the Atmosphere. *Energy Environ. Sci.* **2012**, *5*, 7833–7853.
- (13) Li, B.; Duan, Y.; Luebke, D.; Morreale, B. Advances in CO₂ Capture Technology: a Patent Review. *Appl. Energy* **2013**, *102*, 1439–1447.
- (14) Darunte, L. A.; Oetomo, A. D.; Walton, K. S.; Sholl, D. S.; Jones, C. W. Direct air Capture of CO₂ Using Amine Functionalized MIL-101(Cr). *ACS Sustainable Chem. Eng.* **2016**, *4*, 5761–5768.
- (15) Okunev, A. G.; Sharonov, V. E.; Aristov, Y. I.; Parmon, V. N. Sorption of Carbon Dioxide from Wet Gases by K₂CO₃-in-Porous Matrix: Influence of the Matrix Nature. *React. Kinet. Catal. Lett.* **2000**, *71*, 355–362.
- (16) Liang, Y.; Harrison, D. P.; Gupta, R. P.; Green, D. A.; McMichael, W. J. Carbon Dioxide Capture Using Dry Sodium-Based Sorbents. *Energy Fuels* **2004**, *18*, 569–575.
- (17) Samari, M.; Ridha, F.; Manovic, V.; Macchi, A.; Anthony, E. J. Direct Capture of Carbon Dioxide from Air Via Lime-Based Sorbents. *Mitigation and Adaptation Strategies for Global Change* **2020**, *25*, 25–41.
- (18) Vargas, A.; Külür, A. T.; Wurzbacher, J. A.; Gebald, C. Materials for the Direct Capture of Carbon dioxide from Atmospheric Air. World Intellectual Property Organization; Patent WO 2019/092128 A1, May 16, 2019.
- (19) Zhao, C.; Chen, X.; Zhao, C. Carbonation Behavior and the Reaction Kinetic of a New Dry Potassium-Based Sorbent for CO₂ Capture. *Ind. Eng. Chem. Res.* **2012**, *51*, 14361–14366.
- (20) Pannocchia, G.; Puccini, M.; Seggiani, M.; Vitolo, S. Experimental and Modeling Studies on High-Temperature Capture of CO₂ Using Lithium Zirconate Based Sorbents. *Ind. Eng. Chem. Res.* **2007**, *46*, 6696–6706.
- (21) Barker, R. The Reversibility of the Reaction CaCO₃ CaO +CO₂. *J. Appl. Chem. Biotechnol.* **1973**, *23*, 733–742.
- (22) Li, J.-Z.; Fan, S.-M.; Sun, X.-F.; Liu, S. Nano-K₂CO₃: Preparation, Characterization and Evaluation of Reactive Activities. *RSC Adv.* **2016**, *6*, 1865–1869.
- (23) Nasiman, T.; Kanoh, H. CO₂ Capture by a K₂CO₃–Carbon Composite Under Moist Conditions. *Ind. Eng. Chem. Res.* **2020**, *59*, 3405–3412.
- (24) Yang, G.; Luo, H.; Ohba, T.; Kanoh, H. CO₂ Capture by Carbon Aerogel–Potassium Carbonate Nanocomposites. *Int. J. Chem. Eng.* **2016**, *2016*, 1–8.
- (25) Masoud, N.; Bordanaba-Florit, G.; van Haasterecht, T.; Bitter, J. H. Effect of Support Surface Properties on CO₂ Capture from Air by Carbon-supported Potassium carbonate. *Ind. Eng. Chem. Res. Ind. Eng. Chem. Res.* **2021**, *60*, 13749–13755.

- (26) Kerkhof, F. P. J. M.; Moulijn, J. A. Quantitative Analysis of XPS Intensities for Supported Catalysts. *J. Phys. Chem.* **1979**, *83*, 1612–1619.
- (27) Powell, C. J.; Jablonski, A. *NIST Electron Inelastic-Mean-Free-Path Database*, Version 1.2, SRD 71; National Institute of Standards and Technology: Gaithersburg, MD, 2010.
- (28) Eggenhuisen, T. M.; den Breejen, J. P.; Verdoes, D.; de Jongh, P. E.; de Jong, K. P. Fundamentals of Melt Infiltration for the Preparation of Supported Metal Catalysts. The Case of Co/SiO₂ for Fischer–Tropsch Synthesis. *J. Am. Chem. Soc.* **2010**, *132*, 18318–18325.
- (29) Letellier, P.; Mayaffre, A.; Turmine, M. Melting Point Depression of Nanosolids: Nonextensive Thermodynamics Approach. *Phys. Rev. B* **2007**, *76*, 045428.
- (30) Ueda, T.; Tanaka, T.; Hara, S. Thermodynamic Evaluation of Surface Tension of Molten Salt Mixtures in Alkali Halides, Nitrate, Carbonate and Sulfate Systems. *Zeitschrift Fur Metallkunde* **1999**, *90*, 342–347.
- (31) Ward, A. T.; Janz, G. J. Molten Carbonate Electrolytes: Electrical Conductance, Density and Surface Tension of Binary and Ternary Mixtures. *Electrochim. Acta* **1965**, *10*, 849–857.
- (32) Jayakumar, A.; Gomez, A.; Mahinpey, N. Post-Combustion CO₂ Capture Using Solid K₂CO₃: Discovering the Carbonation Reaction Mechanism. *Appl. Energy* **2016**, *179*, 531–543.
- (33) Jayakumar, A.; Gomez, A.; Mahinpey, N. Kinetic Behavior of Solid K₂CO₃ Under postcombustion CO₂ Capture Conditions. *Ind. Eng. Chem. Res.* **2017**, *56*, 853–863.
- (34) Zhao, C.; Chen, X.; Zhao, C.; Liu, Y. Carbonation and Hydration Characteristics of Dry Potassium-Based Sorbents for CO₂ Capture. *Energy Fuels* **2009**, *23*, 1766–1769.
- (35) Gomez, A.; Jayakumar, A.; Mahinpey, N. Experimental Verification of the Reaction Mechanism of Solid K₂CO₃ During Postcombustion CO₂ Capture. *Ind. Eng. Chem. Res.* **2016**, *55*, 11022–11028.
- (36) Atkins, P.; Overton, T.; Rourke, J.; Weller, M.; Armstrong, F.; Hagerman, M. *Shriver and Atkins' Inorganic Chemistry*; W. H. Freeman and Company: New York, 2010.
- (37) Nguyen, T.-Q.; Glorius, M.; Breitkopf, C. A New Approach to Determine Gas Diffusion Coefficients in Porous Solids by EIS: Application for NH₃ and CO₂ Adsorption on Zirconia and Zeolite Type 5A. *Advances in Mathematical Physics* **2018**, *2018*, 1–11.
- (38) Atkins, P.; Paula, J. D. *Atkins' Physical Chemistry*, 8 ed.; Oxford University Press: New York, 2006.
- (39) Luo, H.; Chioyama, H.; Thürmer, S.; Ohba, T.; Kanoh, H. Kinetics and Structural Changes in CO₂ Capture of K₂CO₃ under a Moist Condition. *Energy Fuels* **2015**, *29*, 4472–4478.
- (40) Redhead, P. A. Thermal Desorption of Gases. *Vacuum* **1962**, *12*, 203–211.
- (41) Melchiori, T.; Canu, P. Improving the Quantitative Description of Reacting Porous Solids: Critical Analysis of the Shrinking Core Model by Comparison to the Generalized Grain Model. *Ind. Eng. Chem. Res.* **2014**, *53*, 8980–8995.
- (42) Lasaga, A. C.; Berner, R. A.; Fisher, G. W.; Anderson, D. E.; Kirkpatrick, R. J. *Reviews in Mineralogy. Kinetics of Geochemical Processes*; Ribbe, P. H., Ed.; De Gruyter: Berlin, 1981; Vol. 8, p 35.
- (43) Veselovskaya, J. V.; Derevschikov, V. S.; Shalygin, A. S.; Yatsenko, D. A. K₂CO₃-containing composite sorbents based on a ZrO₂ aerogel for reversible CO₂ capture from ambient air, Microporous. *Mesoporous. Mater.* **2021**, *310*, 110624.